Advanced Functional Materials

ADVANCED FUNCTIONAL MATERIALS
www.afm-journal.de

RESEARCH ARTICLE

Salt-Bridged Miscibility Unlocks Hydrophobic Diluents to Engineer Anion-Rich Solvation for Highly Reversible Zinc Batteries

Rujian Fu[1] | Bao Li[1] | Shuai Liu[1] | Mengfan Zhao[1] | Xueqing Chen[1] | Lifeng Hou[1,2] | Shi Wang[3,5] | Zhong Jin[4] | Qian Wang[1,2]

[1]College of Materials Science and Engineering, Taiyuan University of Technology, Taiyuan, Shanxi, P. R. China | [2]Shanxi Key Laboratory of Corrosion and Control of Metal Materials, Taiyuan, Shanxi, P. R. China | [3]State Key Laboratory of Flexible Electronics (LoFE) & Institute of Advanced Materials (IAM), Nanjing University of Posts & Telecommunications, Nanjing, P. R. China | [4]State Key Laboratory of Coordination Chemistry, MOE Key Laboratory of Mesoscopic Chemistry, MOE Key Laboratory of High Performance Polymer Materials and Technology, Jiangsu Key Laboratory of Green Energy Catalysis and Intelligent Chemical Engineering, Suzhou Key Laboratory of Green Intelligent Manufacturing of New Energy Materials and Devices, Tianchang New Materials and Energy Technologies Research Center, Institute of Green Chemistry and Engineering, School of Chemistry and Chemical Engineering, Nanjing University, Nanjing, Jiangsu, P. R. China | [5]Yancheng Rouhe Innovative Technology Service Co., Ltd., Yancheng, Jiangsu, P. R. China

Correspondence: Lifeng Hou (houlifeng@tyut.edu.cn) | Shi Wang (iamshiwang@njupt.edu.cn) | Zhong Jin (zhongjin@nju.edu.cn) | Qian Wang (qianwang0825@pku.edu.cn)

Received: 18 March 2026 | **Revised:** 2 June 2026 | **Accepted:** 23 June 2026

Keywords: aqueous zinc batteries | electrolyte | molecular bridges | phase diagram | SEI film

ABSTRACT

Aqueous zinc batteries offer inherent safety and cost advantages, yet their further application is hindered by severe surface corrosion, H_2 evolution. While incorporating organic diluents is a common strategy to modify the electrolyte microenvironment, a fundamental dilemma exists: water-miscible solvents usually have strong Zn^{2+} binding energy, thereby increasing the Zn^{2+} desolvation energy barrier, and even react with Zn metal, whereas inert, hydrophobic diluents fail to form a homogeneous phase. Here, we propose a salt-bridged miscibility mechanism to break through this limitation. Guided by systematic screening, we demonstrate that specific Zn salts, notably $Zn(OTf)_2$, act as efficient molecular bridges, dramatically lowering the miscibility barrier between H_2O and hydrophobic diluents like tetrahydropyran (THP), thereby constructing thermodynamically stable and interface friendly homogeneous electrolyte. The inert THP disrupts the hydrogen bonding network between H_2O molecules, broadens the electrochemical stability window, and participates in interface regulation. As a result, the Zn|Cu half cells employing this engineered inert electrolyte can maintain a high coulombic efficiency of 99.79% over 2000 cycles. And the full cells with HNVO cathode can retain remarkable stability over 30 000 cycles at 5 A g^{-1}. This work solves a fundamental trade-off of hydrophobic diluents for future electrolyte engineering.

1 | Introduction

The escalating demand for grid-scale energy storage and the rapid growth of portable electronics have intensified the exploration for high-safety and low-cost energy storage battery technology [1–6]. Among various candidates, aqueous zinc batteries (ZIBs) stand out due to the natural abundance, high theoretical capacity (820 mAh g^{-1}), and low redox potential (−0.76 V vs SHE) of Zn

Rujian Fu and Bao Li contributed equally to this work.

metal anode, coupled with the inherent non-flammability and high ionic conductivity of aqueous electrolytes [7–10]. However, the practical application of ZIBs is severely hampered by the interfacial instability of Zn metal anode in aqueous media. In conventional aqueous electrolytes, Zn ions are surrounded by H_2O molecules, forming a solvation structure of $[Zn(H_2O)_6]^{2+}$, which triggers continuous parasitic reactions, including corrosive dissolution, H_2 evolution reaction, and the formation of insulating by-products [11–14]. These processes, along with uncontrollable dendrite growth during electrochemical cycling process, lead to rapid capacity fading, low coulombic efficiency and poor cycling lifespan [15–19].

To address these interfacial challenges, the rational design of the Zn^{2+} solvation structure is paramount. A widely adopted strategy to mitigate these issues involves engineering the electrolyte's solvation structure by introducing organic molecules as co-solvents [20–24]. Its main purpose is to displace active H_2O molecules from Zn^{2+} solvation structure of $[Zn(H_2O)_6]^{2+}$, and regulate the hydrogen-bonding network in the bulk electrolyte [25–29]. Nevertheless, this approach presents a fundamental and often overlooked dilemma. On one hand, solvents with high water miscibility typically possess strong Zn^{2+} coordination ability (e.g., ethylene glycol, DMSO), which can create a tightly bound solvation sheath [30–32]. This will inevitably result in an excessively high de-solvation energy barrier for Zn^{2+} ions, kinetically hindering deposition and increasing polarization [33–35]. Moreover, many of these solvents are thermodynamically unstable against the highly reductive Zn metal, especially in the electrochemical cycling process, participating in detrimental side reactions. On the other hand, electrochemically inert, hydrophobic diluents (such as: some cyclic ethers, esters), which could ideally provide a passive interface and even create an anion-rich solvation environment, are largely immiscible with H_2O molecules. In other words, a critical and underexplored gap remains: This inherent hydrophobicity prevents their homogeneous integration into the electrolyte, making them ineffective for uniform solvation structure engineering and leading to bulk phase separation. This critical trade-off between solvent miscibility and interfacial inertness has constrained the design space for high-performance aqueous hybrid electrolytes.

Herein, we propose and validate a novel salt-bridged miscibility strategy to fundamentally resolve this dichotomy. We demonstrate that specific Zn salts can act as molecular bridges, dramatically altering the thermodynamic miscibility between water and incompatible hydrophobic diluents. Through systematic screening of Zn salts (e.g., $ZnSO_4$, $ZnCl_2$, $Zn(OTf)_2$) and diluents, we discover that $Zn(OTf)_2$ can enable the formation of a thermodynamically stable, homogeneous electrolyte with hydrophobic THP. This salt-bridged homogeneous electrolyte achieves multiple synergistic functions: (1) disrupting the hydrogen bonding network between H_2O molecules and broadening the electrochemical stability window; (2) creating an anion-rich solvation structure, formulated as $Zn^{2+}[(H_2O)_{4.5}(THP)_{0.22}(OTf^-)_{1.28}]$ and weakening the Zn^{2+}-H_2O interaction; (3) facilitating the formation of a robust and uniform SEI layer with only ~10 nm thickness, thereby simultaneously enhancing interfacial stability and de-solvation kinetics. As a result, the Zn metal anode exhibits exceptional reversibility, with Zn|Cu half-cells achieving an average Coulombic efficiency (CE) of 99.79% over 2000 cycles. Full cells paired with HNVO cathodes also demonstrate ultra-long cycling life over 30 000 cycles at 5 A g^{-1}. More importantly, even at a low temperature of −20°C, the full cells with PANI cathode can also run stably over 8000 cycles. Beyond presenting a superior electrolyte formula, this work establishes a universal "Zn salt-diluent-H_2O" ternary phase diagram as a predictive tool, shifting the electrolyte design from empirical trial-and-error to rational screening based on salt-mediated miscibility, thereby opening a new avenue for developing stable, high-performance aqueous ZIBs.

2 | Results and Discussion

2.1 | Unlocking Hydrophobic Diluents

Introducing hydrophobic diluents into aqueous electrolytes has proven effective in enriching anion participation within the Zn^{2+} solvation sheath. These diluents share a common characteristic, that is, extremely low dielectric constant and low polarity, leading to limited capacity to dissociate Zn salts. While this characteristic is central to promoting anion association over solvent coordination, it also renders such diluents inherently immiscible with high-dielectric water, aligning with the classic "like dissolves like" principle. This presents a fundamental design conflict: the property desired for solvation tuning creates a thermodynamic barrier to homogeneous electrolyte formulation.

Beyond polarity, molecular architecture, including hydrophilic/hydrophobic moieties, steric bulk, and molecular size, further dictates miscibility. As shown in Figure 1a and Table S1, we systematically evaluated several low-ε diluents. Slight structural changes led to remarkable changes in their water solubility, which underwent spontaneous aggregation and phase separation—a manifestation of the hydrophobic effect (Figure S1). According to previous research, this effect was driven by water's tendency to maximize its own cohesive hydrogen-bonding network, effectively "expelling" non-polar solutes. Based on this, a key design insight emerged: disrupting the hydrogen bonds among bulk water molecules should weaken this exclusionary force, thereby enhancing the compatibility of hydrophobic diluents [36, 37]. First, as shown in Figure 1b and Figure S2, based on the dielectric constant, the HOMO-LUMO gap energy and the oil-water partition coefficient (Log P) of solvent molecules were further used to screen inert diluents. These two parameters are employed to evaluate the electrochemical stability and hydrophobicity of solvents, respectively. Among these solvents, THP exhibits a relatively high energy gap value (7.96 eV), indicating strong redox stability. It also possesses the highest LUMO level (1.14 eV), demonstrating the greatest resistance to reduction stability and thus the highest inertness at the anode surface. Additionally, THP has a Log *p*-value of 1.21, reflecting the strongest hydrophobicity, which is beneficial for the formation of a hydrophobic interface at the zinc anode. Ultimately, THP was selected for further exploration.

Then, we investigated the capacity of various anions—known to differentially perturb water structure, to mediate the dissolution of THP. As shown in Figure S3, while Zn salts like $ZnSO_4$, $Zn(BF_4)_2$, $ZnCl_2$, $Zn(ClO_4)_2$, and $Zn(OTf)_2$ exhibited almost no solubility in THP, their presence in water dramatically

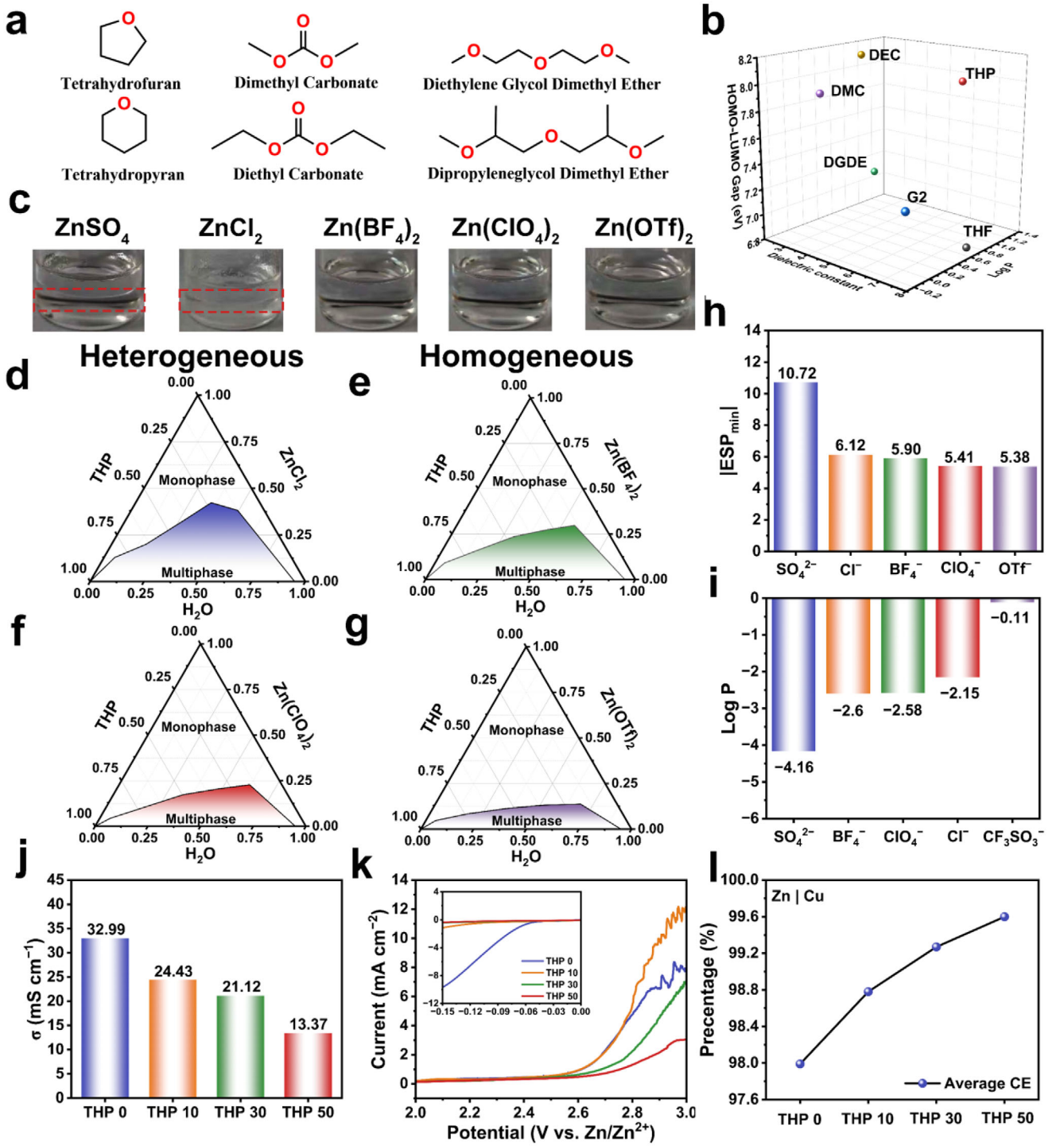

FIGURE 1 | Unlocking hydrophobic diluents. (a) Structural formulas of some organic solvents with low dielectric constant; (b) Comparison of dielectric constant, oil-water partition coefficient, and HOMO-LUMO Gap energy among different solvents; (c) Optical photograph of 2 M Zn salt solutions containing 50 vol.% THP; (d–g) ternary phase diagrams for the H_2O/THP system with $ZnCl_2$, $Zn(BF_4)_2$, $Zn(ClO_4)_2$, and $Zn(OTf)_2$, respectively; (h) Electrostatic potential maps of different anions; (i) Corresponding oil-water partition coefficient (Log P) values of the anions; (j) Ionic conductivity of electrolytes with varying THP content; (k) LSV curves showing the suppression of hydrogen evolution and the broadening of the electrochemical stability window upon THP introduction; (l) Average CE of Zn|Cu half-cells employing different electrolytes.

altered THP miscibility. As shown in Figure 1c, under the same concentration (2.0 M) and proportion (50% THP) conditions, BF_4^-, ClO_4^-, and OTf^- fostered homogeneous phases, whereas SO_4^{2-} and Cl^- led to clear separation. Subsequently, ternary phase diagrams obtained by cloud point titration were used to more precisely compare the influence of different anions on THP dissolution. As shown in Figure 1d–g and Figure S4, the results demonstrated a contracting multiphase region in the order: SO_4^{2-}<Cl^-< BF_4^-<ClO_4^-< OTf^-, which was related to the electrostatic potential of anions and their tendency to disrupt

water's hydrogen-bonding network. As shown in Figure 1h and Figure S5, the anions positioned toward the right side were more inclined to disrupt the water structure, thereby facilitating THP dissolution. Furthermore, the exceptional efficacy of the OTf^- anion was attributed to its amphiphilic structure and superior lipophilicity. As shown in Figure 1i, the Log *p*-values corresponding to different anions confirmed that the OTf^- anion possessed stronger lipophilicity, enabling it to act as a molecular bridge between the aqueous and organic phases. Additionally, as shown in Figures S6–S8, several hydrophobic diluents (DMC, DGDE, and MA) were also employed to validate the "salt bridge effect" mechanism. Ternary phase diagrams of the "Zn salt–diluent–H_2O" systems for these solvents demonstrate that this mechanism has a certain degree of universality.

Considering the strong molecular bridge capability and its tendency to promote the formation of stable SEI layer, $Zn(OTf)_2$ was selected as the optimal Zn salt for constructing a homogeneous electrolyte with THP. Then, we prepared a series of electrolytes with varying THP content (named as: THP X, where X is the THP vol.%), which was shown in Figure S9. A homogeneous phase was maintained up to 70% THP, beyond which salt dissolution was incomplete. Meanwhile, the ionic conductivity gradually decreased with increasing THP proportion, and THP 50 still retained a high ionic conductivity of 13.37 mS cm^{-1} (Figure 1j and Figure S10). Critically, linear sweep voltammetry (LSV) demonstrated that THP introduction significantly suppressed H_2 evolution and widened the electrochemical stability window (Figure 1k). Furthermore, Zn | Cu half-cells were assembled to evaluate the reversibility of different electrolytes. As shown in Figure 1l and Figure S11, THP 50 displayed the highest average CE and longest cycling life. Based on the above analysis, THP 50 was identified as optimal and selected for all subsequent research.

2.2 | Analysis of Electrolyte Structure

The microstructure of the electrolyte was analyzed in detail through Fourier-transform infrared (FTIR) spectroscopy, Raman spectroscopy, and nuclear magnetic resonance (NMR) spectroscopy, combined with molecular dynamics (MD) simulations and density functional theory (DFT) calculations. The impact of salt-bridged miscibility strategy on the hydrogen-bonding network was first evident in FTIR spectra. As shown in Figure 2a, the characteristic -OH stretching vibration (3385 cm^{-1}) and bending vibration (1631 cm^{-1}) exhibited pronounced blueshifts upon THP addition, signifying a disruption of the hydrogen-bonding network among water molecules, thus effectively reducing their activity. Correspondingly, the ^1H NMR spectra gradually shifted from high field to low field, further confirming the reconstruction of the bulk water structure (Figure 2b).

Then, we further investigated the state of anions in the electrolyte. As shown in Figure S12, the FTIR peak corresponding to the $-SO_3$ group (1034.04 cm^{-1}) shifted to a higher wavenumber, indicating a strengthened interaction between OTf^- and Zn^{2+}. Furthermore, Raman spectral deconvolution of the OTf^- characteristic peak provided quantitative insight: with increasing THP content, the proportion of contact ion pairs (CIP) rose markedly at the expense of solvent-separated ion pairs (SSIP), indicating that anions progressively replaced water molecules in the solvation shell, which was beneficial for suppressing side reactions induced by water molecules and promoting the formation of a stable SEI (Figure 2c). Besides, the ^{19}F NMR signal exhibited a downfield shift, reflecting a de-shielding effect on the OTf^- anion due to enhanced Zn^{2+} coordination (Figure 2d), a finding further supported by FTIR analysis (Figure S13).

DFT calculations provided energetic validation of these interactions. As shown in Figure 2e, the binding energy between THP and H_2O (−0.3654 eV) was found to be stronger than that between H_2O molecules (−0.3146 eV), indicating that the salt-bridged miscibility strategy can disrupt the hydrogen bonding network of water, which was consistent with spectroscopic results. Moreover, Zn^{2+} and OTf^- exhibited the highest binding energy, suggesting a stronger tendency for coordination between them, while the introduction of hydrophobic THP can further enhance their interaction.

The coordination environment of Zn^{2+} was further analyzed via MD simulations. Figure 2f–i shows the MD simulation snapshots and corresponding radial distribution functions (RDF) for the baseline (THP 0) and optimal (THP 50) electrolytes. In the pure aqueous system, Zn^{2+} was primarily coordinated by 5.35 H_2O molecules and only 0.65 OTf^- anions, yielding a water-rich $[Zn(H_2O)_{5.35}(OTf^-)_{0.65}]$ solvation structure. In striking contrast, owing to the salt-bridged miscibility strategy, the H_2O coordination number in the THP 50 electrolyte decreased to 4.50, while the OTf^- coordination number increased significantly to 1.28. THP itself showed minimal coordination (only 0.22), confirming its role as a non-coordinating diluent. Furthermore, the number of hydrogen bonds in the two systems was calculated. As shown in Figure 2j, the addition of THP reduced the number of hydrogen bonds in the electrolyte, effectively disrupting the continuous hydrogen-bond network among water molecules.

Finally, we probed the kinetic behavior under the influence of the salt-bridged miscibility strategy. Electrochemical impedance spectroscopy (EIS) was performed at different temperatures, and the activation energy (E_a) for THP 0 and THP 50 electrolytes was fitted using the Arrhenius equation. As shown in Figure 2k and Figure S14, the THP 50 electrolyte possessed both a lower charge-transfer resistance (R_{ct}) and a significantly reduced activation energy (20.44 kJ mol^{-1}), indicating faster Zn^{2+} kinetics. To summarize briefly, the salt-bridged miscibility strategy helped to successfully engineer an anion-rich solvation sheath of $Zn^{2+}[(H_2O)_{4.5}(THP)_{0.22}(OTf^-)_{1.28}]$. It achieved the dual critical objectives of passivating active water and enriching the interface with anions, which not only mitigated parasitic reactions but also facilitated the formation of a stable SEI layer and faster Zn^{2+} deposition kinetics.

2.3 | Interface Analysis and SEI Layer

The long-term cycling stability of Zn metal anodes is fundamentally governed by the electrode-electrolyte interfacial chemistry. We therefore systematically investigated how the salt-bridged miscibility strategy mitigates corrosion and regulates the formation of SEI film. The linear polarization (Tafel) curves were first employed to investigate the corrosion behavior. As shown in Figure 3a, the THP 50 electrolyte exhibited a significantly more

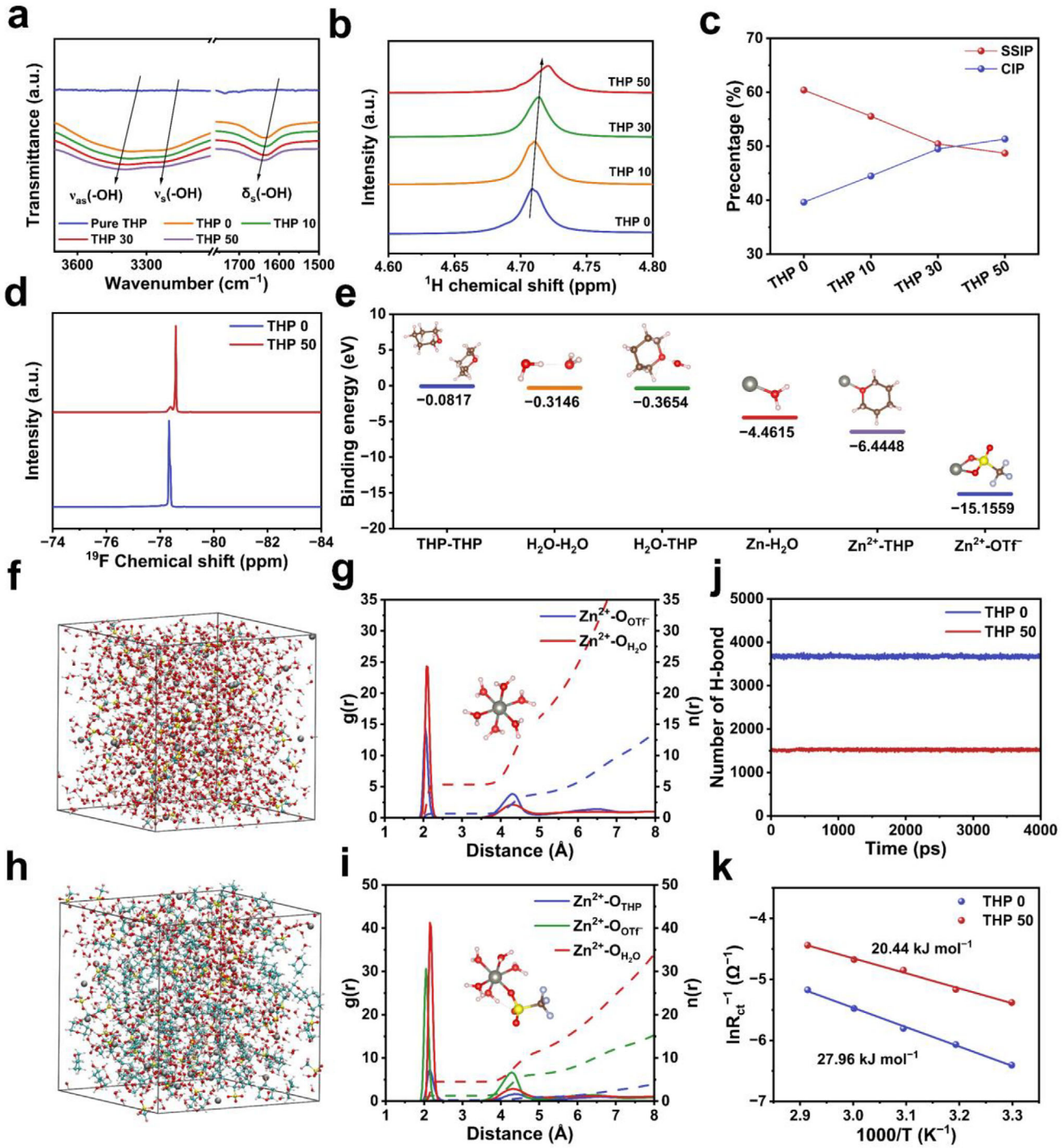

FIGURE 2 | Structural Analysis of Electrolytes. (a) FTIR spectra of the O–H stretching and bending regions in different electrolytes; (b) ^{1}H NMR spectra of different electrolytes; (c) Proportion of CIP and SSIP from Raman spectral deconvolution; (d) ^{19}F NMR spectra of different electrolytes; (e) DFT-calculated binding energies among key components; (f) MD simulation snapshot of THP 0 electrolyte; (g) RDF and derived solvation structure model of THP 0 electrolyte; (h) MD simulation snapshot of THP 50 electrolyte; (i) RDF and derived solvation structure model of THP 50 electrolyte; (j) Comparison of the number of hydrogen bonds in THP 0 and THP 50 electrolytes obtained from MD; (k) De-solvation energy (E_a) of THP 0 and THP 50 electrolytes fitted by the Arrhenius equation.

positive corrosion potential (−0.002 V) and a lower corrosion current density compared to the THP 0 baseline, indicating markedly suppressed anodic corrosion. Correspondingly, SEM images of Zn foils after immersing in the THP 0 electrolyte showed substantial surface passivation by-products, identified via XRD as $Zn_x(OTf)_y(OH)_{2x-y}\cdot nH_2O$ (Figure S15). In contrast, the Zn surface remained smooth and clean in the THP 50 electrolyte, directly linking the reduction of active water in the solvation shell to inhibited corrosion. Besides, AC voltammetry was also used to probe changes in the electrical double layer (EDL) in the interfacial microenvironment. As shown in Figure 3b, the introduction of THP resulted in a decreased interfacial capacitance,

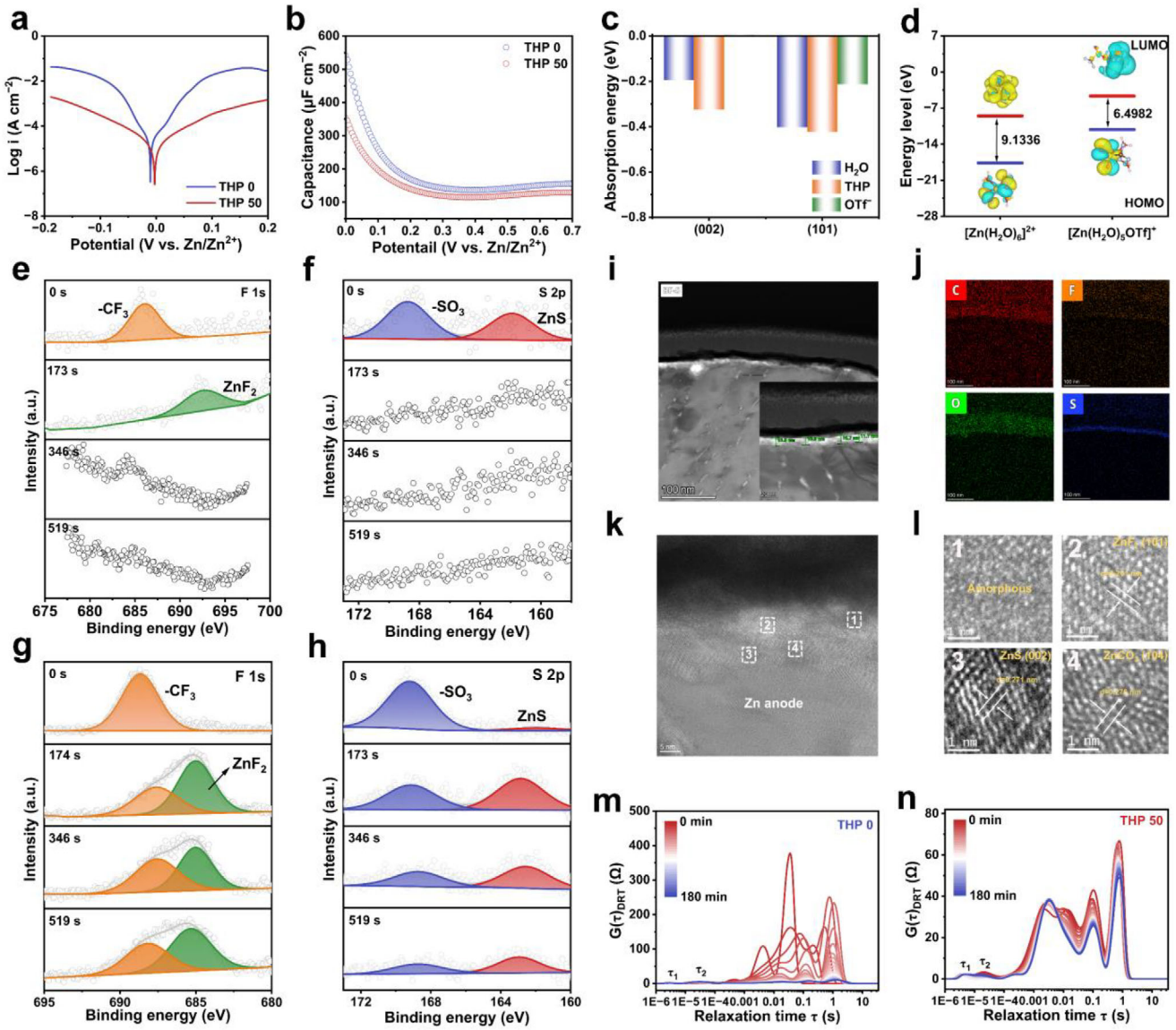

FIGURE 3 | Interface stability and SEI film. (a) Tafel polarization curves of THP 0 and THP 50 electrolytes; (b) Differential capacitance tests of THP 0 and THP 50 electrolytes using Zn|Ti half-cells; (c) DFT-calculated adsorption energies of H_2O, THP, and OTf^- on Zn (101) and (002) surfaces; (d) HOMO and LUMO energy levels of $[Zn(H_2O)_6]^{2+}$ and $[Zn(H_2O)_5(OTf^-)]^+$ structures; (e,f) Depth-profiling XPS spectra of the SEI formed in different electrolyte systems, (e) F 1s and (f) S 2p; (g,h) Corresponding XPS depth profiles for the SEI, (g) F 1s and h) S 2p; (i) TEM images of the SEI formed in THP 50 electrolyte; (j) EDS elemental mapping (C, O, F, S, Zn) confirming the uniform composition of the SEI; (k, l) HRTEM images with lattice fringes corresponding to ZnF_2, ZnS, and $ZnCO_3$ within the SEI; (m, n) DRT plots for THP 0 and THP 50 electrolyte systems.

suggesting the adsorption of THP molecules onto the Zn surface. The introduction of THP shifted the zeta potential positively, indicating that THP, with its low dielectric constant, weakened the polar environment of water and directly adsorbs onto the zinc surface, thereby collectively "neutralizing" or "screening" the original negative charge on the zinc surface (Figure S16). Subsequently, the adsorption energies of H_2O, OTf^-, and THP on various Zn crystal planes were calculated. As shown in Figure 3c, the adsorption energies of THP on both the Zn(002) and (101) crystallographic planes were substantially higher than those of H_2O or OTf^-. Corresponding differential charge density analysis revealed significant electron cloud redistribution upon THP adsorption, further corroborating the adsorption of THP on the anode surface (Figure S17). Consequently, this preferential adsorption established a hydrophobic molecular layer at the interface, physically displacing water molecules and further mitigating contact-induced corrosion.

The stability of the interface is ultimately dictated by the SEI. The anion-rich solvation structure of $Zn^{2+}[(H_2O)_{4.5}(THP)_{0.22}(OTf^-)_{1.28}]$ modulated by THP, created favorable conditions for the formation of a uniform SEI layer. Multi-scale characterization was employed to reveal the structure of the SEI formed in different electrolytes. First, DFT calculations indicated that the energy gap between the HOMO and LUMO for the $[Zn(H_2O)_5(OTf)]^+$ complex (6.50 eV) was significantly smaller than that for $[Zn(H_2O)_6]^{2+}$ (9.13 eV), indicating a higher reducibility of OTf^- within the solvation

sheath and its thermodynamic propensity to form the SEI (Figure 3d).

Depth-profiling XPS analysis provided direct evidence of SEI composition and homogeneity. As shown in Figure 3e,f, for the Zn metal anode cycled in the THP 0 electrolyte, the SEI components were heterogeneous and largely confined to the outermost surface. In stark contrast, the SEI formed in the THP 50 electrolyte exhibited remarkable uniformity and depth penetration. Even after 519 s of Ar^+ sputtering, strong signals for inorganic species (ZnF_2, ZnS) and organic moieties ($-CF_3$, $-SO_3$) from OTf^- decomposition were clearly detected (Figure 3g,h). Furthermore, the C 1s and O 1s spectra confirmed the presence of $ZnCO_3$ and $-CF_3$ components within the SEI formed in the THP 50 electrolyte (Figure S18). This homogeneous, deep-distributed hybrid structure contrasted with the THP 0 electrolyte system, where the O 1s spectrum was dominated by $ZnO/Zn(OH)_2$, indicating severe parasitic reactions. Quantitative analysis of the high-resolution XPS depth profiles also showed that upon introduction of THP, the F and S contents in the SEI layer significantly increased and remained uniformly distributed with increasing etching depth (Figure S19). Furthermore, TEM and high-resolution TEM (HRTEM) unveiled the nanoscale morphology and crystallography of this robust SEI. As shown in Figure 3i,j, a continuous and dense SEI layer of ~10 nm thickness was observed, with elemental mapping confirming a uniform distribution of C, O, F, S, and Zn. Meanwhile, HRTEM images revealed the lattice fringes corresponding to ZnF_2, ZnS, and $ZnCO_3$, confirming the formation of an inorganic–organic hybrid SEI layer. This hybrid SEI layer not only ensures a certain level of ion transportability, but also the presence of organic species endows it with a degree of flexibility and self-healing capability [38–40].

The dynamic stability of this interface was also monitored by in situ EIS. As shown in Figure S20, during continuous Zn deposition, the charge transfer resistance (R_{ct}) for both electrolytes gradually stabilized. However, the cells using the THP 0 electrolyte system experienced an abrupt decrease in R_{ct} due to an internal short circuit. At the same time, the corresponding distribution of relaxation times (DRT) analysis offered further insight. As shown in Figure 3m,n, during the initial deposition cycles, the time constant τ_2 associated with the SEI resistance exhibited remarkable stability in the THP 50 electrolyte system, whereas it showed a significant increase in the THP 0 electrolyte system (Figure S21). Additionally, longer-term in situ EIS measurements were performed (Figure S22). Over 20 cycles, THP 50 maintained a more stable R_{ct}. The dynamic evolution of the SEI layer was also analyzed. The τ_2 peak corresponding to R_{SEI} in THP 0 was irregularly distributed, further indicating the instability of the SEI layer. In contrast, the R_{SEI} of THP 50 gradually stabilized during cycling.

2.4 | Zn Deposition Behavior and Cycling Stability

The interfacial properties engineered by the salt-bridged miscibility strategy extend beyond corrosion suppression to fundamentally regulate Zn deposition behavior and overall cell performance. The low dielectric constant of THP enhanced the electrolyte wettability on the Zn surface, as evidenced by a substantial decrease in contact angle from 52.13° to 19.51° (Figure S23), promoting a more homogeneous distribution of the interfacial electric field, which was critical for uniform Zn^{2+} flux and nucleation. Subsequently, Chronoamperometry (CA) was employed to analyze the nucleation mode at the initial deposition stage.

As shown in Figure 4a, upon applying a −150 mV overpotential, the THP 0 electrolyte exhibited a sharp current transient, indicating a typical 2D diffusion process, which was associated with localized "tip effects." In contrast, the THP 50 electrolyte showed a more gradual current rise, characteristic of progressive nucleation and 3D diffusion, signaling a more uniform ion distribution and nucleation site availability. Furthermore, cyclic voltammetry (CV) revealed a higher nucleation overpotential in the THP 50 electrolyte system, which favored the formation of a larger number of finer nucleation sites, leading to a denser deposit (Figure 4b).

Then, the impact on deposition morphology was visualized via SEM. After depositing 1 mAh cm^{-2} of Zn on Cu substrates, the deposits from THP 0 electrolyte exhibited an irregular and non-uniform morphology with exposed substrate areas, whereas THP 50 electrolyte system yielded a compact and uniform layer composed of fine grains across various current densities (Figure 4c,d). The crystallographic orientation of Zn deposits in different electrolytes was analyzed by XRD, which was shown in Figure 4d and Figure S24. Both electrolytes showed a similar crystallographic preference, with a transition from the Zn(101) to the Zn(002) plane as the current density exceeded 10 mA cm^{-2}. Crucially, the XRD pattern for the THP 0 electrolyte system showed distinct peaks corresponding to parasitic by-products, which were virtually absent in the THP 50 electrolyte system, underscoring its effectiveness in suppressing side reactions during plating (Figure 4e).

The high interfacial stability and deposition uniformity directly translated into exceptional electrochemical performance. Zn||Zn symmetric cells with the THP 50 electrolyte demonstrated remarkable rate capability and long-term cycling stability, maintaining stable polarization for over 2000 h at 5.0 mA cm^{-2} (Figure 4f) and 350 h even at an ultra-high current density of 30 mA cm^{-2} (Figure 4h). In stark contrast, unstable voltage polarization was observed during cycling when using the THP 0 electrolyte system and even failed after less than 400 h, attributed to non-uniform deposition leading to internal short circuits (Figure 4g). Furthermore, SEM images of electrodes after 100 plating/stripping cycles revealed a much smoother and denser surface for the THP 50 electrolyte system, while the electrode cycled in the THP 0 electrolyte was riddled with pits and vertically aligned dendrites, significantly shortening its cycle life (Figure S25). Meanwhile, AFM images also confirmed a significantly flatter and more uniform surface topography for Zn deposition in the THP 50 electrolyte system (Figure S26).

The reversibility of Zn plating/stripping was also analyzed in Zn|Cu half-cells. As shown in Figure 4i, the THP 50 electrolyte enabled over 2000 cycles at 5.0 mA cm^{-2} with an exceptional average CE of 99.79%, while the cells cycled in the THP 0 electrolyte system failed after ~30 cycles with a lower average CE. The corresponding specific capacity-voltage profiles were

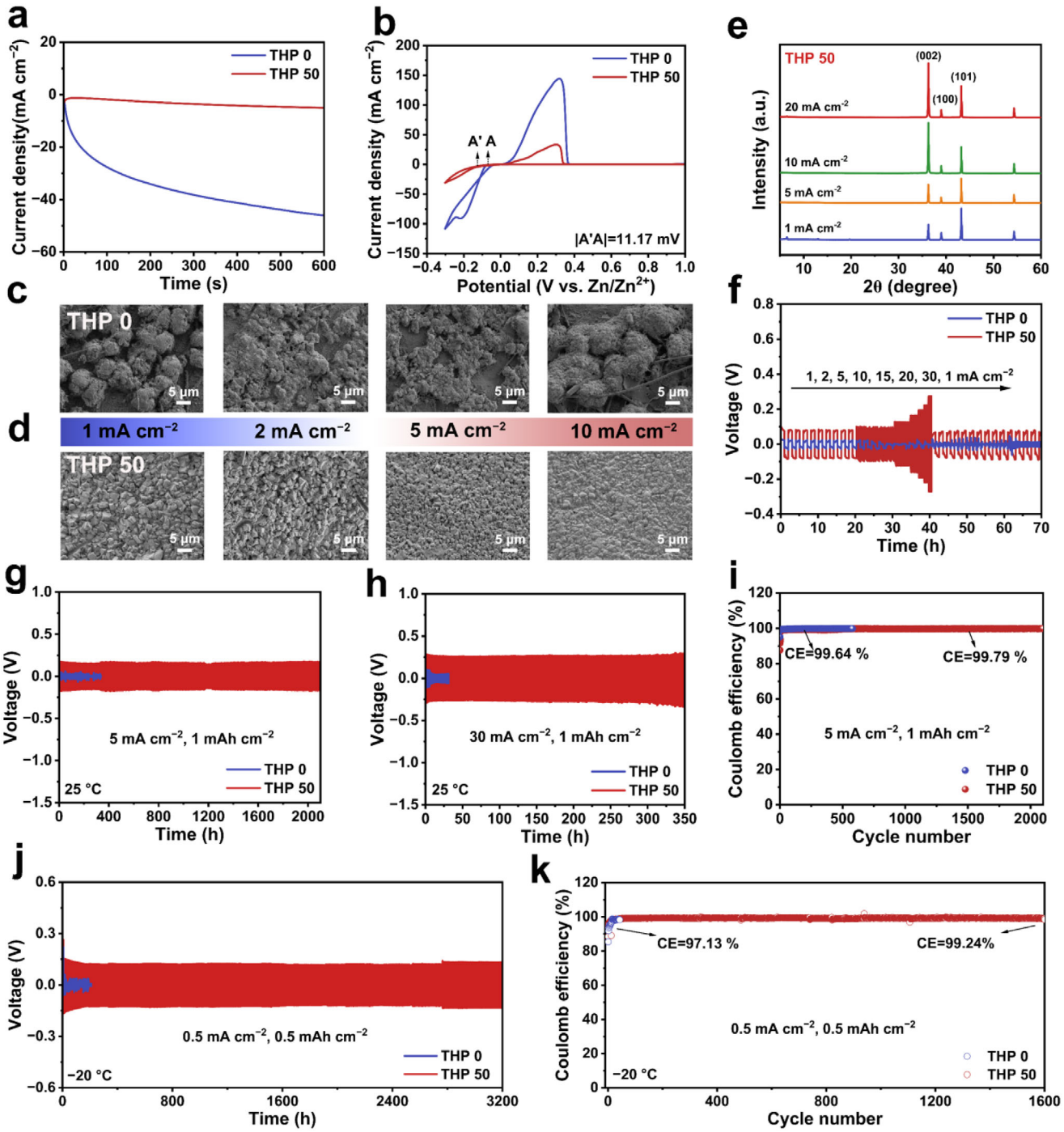

FIGURE 4 | Zn deposition behavior and cycling stability. (a) Chronoamperometry (CA) responses at −150 mV on Zn foil in different electrolytes; (b) CV curves of Zn|Cu half cells in THP 0 and THP 50 electrolytes; (c,d) SEM images of Cu substrates after 1 mAh cm^{-2} Zn deposition in THP 0 and THP 50 electrolytes at different current density; (e) XRD patterns of Zn deposits from THP 50 electrolyte after 100 cycles at different current densities (1–20 mA cm^{-2}); (f) Rate performance of Zn || Zn symmetric cells in THP 0 and THP 50 electrolytes; (g, h) Long-term cycling of Zn||Zn symmetric cells at 5 mA cm^{-2}, 1 mAh cm^{-2} (g) and 30 mA cm^{-2}, 1 mAh cm^{-2} (h), respectively; (i) Cycling performance and CE of Zn|Cu half-cells at 5 mA cm^{-2}, 1 mAh cm^{-2}; (j, k) Low-temperature (−20°C) performance of Zn||Zn symmetric cells (j) and Zn|Cu half-cells (k) at 0.5 mA cm^{-2}, 0.5 mAh cm^{-2}.

also provided in Figure S27. Leveraging the lower freezing point of the salt-bridged miscibility strategy, we further evaluated its low-temperature performance (Figure S28). Although the ionic conductivity of THP 50 was slightly lower than that of THP 0 when the temperature decreases to −20°C, it exhibited a much lower R_{ct} (Figure S29). As shown in Figure 4j,k, at −20°C, the cells using the THP 50 electrolyte delivered a significantly longer cycle life (over 3200 h for Zn || Zn) and superior reversibility (average CE = 99.24% for Zn | Cu), significantly outperforming the THP 0 electrolyte baseline. Simultaneously, SEM images showed that compared to the disordered and porous deposition morphology in the THP 0 electrolyte system, the THP 50 electrolyte yielded

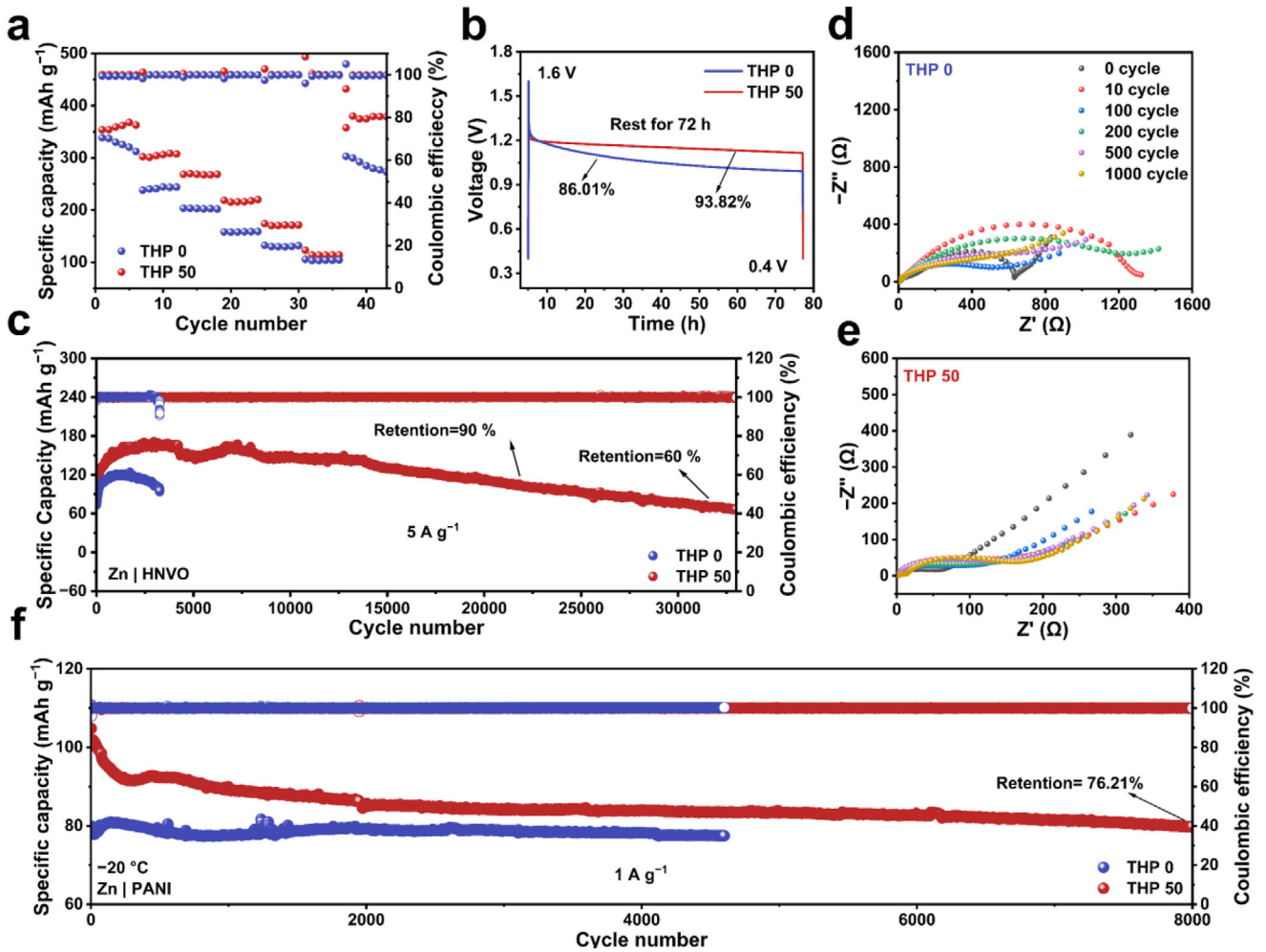

FIGURE 5 | Full cells and application. (a) Rate capability of the Zn||HNVO full cell; (b) Self-discharge test of Zn||HNVO full cells in THP 0 and THP 50 electrolytes; (c) Cycling performance of the Zn||HNVO full cell at 5 A g^{-1}; (d,e) EIS spectra of THP 0 and THP 50 electrolytes at different cycle numbers under 5 A g^{-1}; (f) Cycling performance of the Zn||PANI full cell at −20°C and 1 A g^{-1}.

a dense and well-stacked platelet-like morphology, highlighting its promising application potential under extreme environmental conditions (Figure S30).

2.5 | Full Cells and Application

To comprehensively assess the practical application of the salt-bridged miscibility strategy, full cells were assembled with high-performance cathodes. As shown in Figure 5a and Figure S31, the Zn||HNVO full cells employing the THP 50 electrolyte delivered superior rate capability, with specific discharge capacities of 362.9, 307.6, 268.5, 220.1, 171.4, and 113.9 mAh g^{-1} at current densities ranging from 0.1 to 5 A g^{-1}, significantly outperforming the baseline THP 0 electrolyte. At the same time, the capacity recovered to 357.9 mAh g^{-1} when the current density was returned to 0.1 A g^{-1}, demonstrating excellent reversibility. Furthermore, a storage test was conducted to evaluate the self-discharge behavior of the ZIBs. As shown in Figure 5b, the cells with THP 50 electrolyte maintained a capacity retention of 93.82% after 72 h of open circuit storage, whereas the capacity retention for the THP 0 electrolyte system dropped to 86.01%, indicating its robust charge retention capability.

Subsequently, the long cycling performance of the Zn||HNVO full cells was evaluated at 5 A g^{-1}, which was shown in Figure 5c. The cell employing THP 50 electrolyte sustained stable operation for over 30 000 cycles, retaining 90% of its initial capacity after 20 000 cycles and 60% after 30 000 cycles, a performance far exceeding that of the THP 0 electrolyte system. Compared with recent studies, the full-cell performance of the THP 50 electrolyte based on the "salt-bridge effect" mechanism is among the most excellent (Table S2). EIS spectra collected at different cycle numbers revealed that the cells using the THP 50 electrolyte maintained lower and more stable interfacial impedance throughout this ultra-long cycling, further confirming its exceptional stability during prolonged cycling (Figure 5d,e). The battery also exhibited stable cycling performance at a low current density (0.1 A g^{-1}), maintaining a capacity retention rate of 84.69% after 700 cycles, indicating that it possessed excellent stability during long-term operation at low rates. (Figure S32). In practical applications, it is often necessary to pair with high-loading cathodes to achieve high areal capacity designs. In practical applications, it is often necessary to pair with high-loading cathodes to achieve high areal capacity designs. As shown in Figure S33, when the cathode loading was increased to 10.61 mg cm^{-2}, an initial areal capacity of 1.15 mAh cm^{-2} was obtained, which decayed by

only approximately 0.01 mAh cm^{-2} after 400 cycles. Meanwhile, replacing $Zn(OTf)_2$ with $Zn(ClO_4)_2$ or $Zn(BF_4)_2$ while pairing with the cathode still yields reasonable cycling performance (Figure S34). Furthermore, using DMC, DGDE, or MA as diluents with different zinc salts serving as the "molecular bridge" enables stable operation when paired with HNVO and PANI cathode materials, demonstrating excellent scalability (Figures S35–S37).

To verify the low temperature performance, a Zn||PANI full cell was tested at −20°C. The excellent kinetics also ensure that THP 50 exhibits better rate performance at low temperatures (Figure S38). As shown in Figure 5f, the THP 50 electrolyte enabled a high initial capacity of 104.8 mAh g^{-1} at 1.0 A g^{-1} and maintained 76.2% capacity retention after 8000 cycles. In stark contrast, the cells using the THP 0 electrolyte demonstrated lower capacity and failed after only approximately 4000 cycles. At low temperatures, voltage hysteresis caused by sluggish kinetics can lead to severe capacity decay and accelerated aging. As shown in Figure S39, when the temperature decreases to −20°C, the capacity decay of THP 0 system was more severe than that of THP 50 system. As shown in Figure S40, at −20°C, THP 50 system consistently exhibited narrower charge/discharge hysteresis than THP 0 system during the first, 100th, and 1000th cycles, corresponding to both lower polarization and superior kinetic stability during prolonged cycling. These results conclusively demonstrate that the electrolyte engineered via the "salt-bridged miscibility" mechanism not only achieves breakthrough stability in electrolyte system and interface but also enables durable, high-performance, and wide-temperature-range operation in practical full-cells.

3 | Conclusion

In summary, this work demonstrates a highly effective electrolyte design for ZIBs, leveraging the synergistic interplay between amphiphilic OTf^- anions and a hydrophobic THP. The central innovation lies in the "salt-bridged miscibility" mechanism, which overcomes the inherent thermodynamic barrier to dissolving inert diluents in water, thereby enabling precise solvation engineering. This approach successfully transforms the Zn^{2+} solvation environment from a conventional water-dominated structure into an optimized and anion-rich configuration. This structural reconfiguration delivers multifaceted benefits at the Zn anode interface. The significant reduction of active water in the solvation shell directly suppresses hydrogen evolution and corrosion. Concurrently, the enriched OTf^- anions facilitate faster Zn^{2+} de-solvation kinetics, and, crucially, guide the preferential reduction of anions during plating, thereby forming a thin (~10 nm), uniform and hybrid SEI film. Beyond the solvation sheath, THP preferentially adsorbs on the Zn surface, restructuring the electrical double layer to further exclude water and guiding uniform Zn^{2+} flux, resulting in dense and dendrite-free Zn deposition even at high rates and low temperatures. Consequently, the engineered electrolyte enables ultra-stable Zn plating/stripping over 2000 h in symmetric cells, highly reversible cycling with an average CE>99.79% in Zn|Cu half-cells, and outstanding full-cell cycling life exceeding 30 000 cycles at 5 A g^{-1} with the HNVO cathode. This work introduces "salt-bridged miscibility" as a general design principle and provides the ternary "salt-diluent-water" phase diagram as a predictive tool, opening a new avenue for developing durable, high-performance energy storage systems.

Acknowledgements

This work was supported by the National Natural Science Foundation of China (Nos. 22402146, 22572140, U24A6002, U25A20628, 22561160129, 22479074, 22475096, 52533008), the Equipment Pre-Research and Ministry of Education Joint Fund (8091B02052407), the Fundamental Research Program Key Project of Jiangsu Province (BK20253008), the Science and Technology Major Project of Jiangsu Province (BG2024013), the Scientific and Technological Achievements Transformation Special Fund of Jiangsu Province (BA2023037), the Academic Degree and Postgraduate Education Reforming Project of Jiangsu Province (JGKT24_C001), the Key Core Technology Open Competition Project of Suzhou City (SYG2024122), the Open Research Fund of Suzhou Laboratory (SZLAB-1308-2024-TS005), the Chenzhou National Sustainable Development Agenda Innovation Demonstration Zone Provincial Special Open Competition Project (2023sfq11, 2025sfq38), and the Fundamental Research Funds for the Central Universities and Nanjing University International Collaboration Initiative (020514380354). Open Research Fund of Guangdong Advanced Carbon Materials Co., Ltd. (Kargen-2024B0905), the special fund for Science and Technology Innovation Teams of Shanxi Province (202204051001004), the National Natural Science Foundation of NJUPT (NY223079, NY224119), the Yanlong Lake Science and Technology Development Program.

Conflicts of Interest

The authors declare no conflicts of interest.

Data Availability Statement

The data that support the findings of this study are available from the corresponding author upon reasonable request.

References

1. R. Fu, B. Zhang, T. Lu, et al., "A Dilute and Non-Flammable Electrolyte Engineering Enables Stable SEI for Low-Temperature Zinc Batteries," *Energy Storage Materials* 80 (2025): 104374, https://doi.org/10.1016/j.ensm.2025.104374.

2. B. Li, B. Zhang, X. Bai, et al., "A Dynamic Self-Healing Protective Layer Enabling Stable Zinc Ion Batteries through Strong Zn-S Affinity and Intramolecular Hydrogen Bonding," *Angewandte Chemie International Edition* 64 (2025): 202503345.

3. M. Zhao, B. Zhang, X. Bai, et al., "Competitive Li^+ Coordination in Gel Electrolyte Enhances Zn^{2+} Kinetics and Interfacial Stability for Low-Temperature Zn-Ion Batteries," *Chemical Engineering Journal* 520 (2025): 166042, https://doi.org/10.1016/j.cej.2025.166042.

4. S. Tang, Q. Wei, B. Liu, et al., "Simultaneous Manipulation of Electric Double Layer and Zn (100) Deposition Enabled by Anions for Highly Stable Zn Anodes," *Angewandte Chemie International Edition* 64 (2025): 202510252, https://doi.org/10.1002/anie.202510252.

5. L. Zhang, M. Lin, Z. Yu, et al., "Tyrosine Additives With Rich-Polar Functional Groups Provide Multi-Protections for Ultra-Stable Zinc Metal Anodes," *Energy Storage Materials* 75 (2025): 104022, https://doi.org/10.1016/j.ensm.2025.104022.

6. Z. Peng, S. Li, L. Tang, J. Zheng, L. Tan, and Y. Chen, "Water-Shielding Electric Double Layer and Stable Interphase Engineering for Durable Aqueous Zinc-Ion Batteries," *Nature Communications* 16 (2025): 4490, https://doi.org/10.1038/s41467-025-59830-y.

7. X. Chen, C. Liu, X. Bai, et al., "A Thin and Homogeneous Solid Electrolyte Interface Enriched With ZnF_2 and ZnS for Highly Reversible

Zinc Batteries," *Energy Storage Materials* 75 (2025): 103984, https://doi.org/10.1016/j.ensm.2024.103984.

8. B. Wu, T. Lu, X. Bai, et al., "Dual-Induced Directed Deposition Mechanism Based on Anionic Surfactants Enables Long Cycle Aqueous Zinc Ion Batteries," *Small Methods* 9 (2025): 2401838, https://doi.org/10.1002/smtd.202401838.

9. T. Lu, S. Wang, C. Liu, et al., "Inverse Solvation Configuration Induced by Organic Small-Molecule Spatially-Confined Coordination Enables Highly Reversible Zinc Batteries," *Advanced Functional Materials* 36 (2025): 23416.

10. C. Liu, B. Zhang, Z. Liang, et al., "Synergistically Modulating the Inner Helmholtz Plane and Outer Helmholtz Plane to Achieve a Stable Interface for Aqueous Zinc Ion Batteries," *Chemical Engineering Journal* 508 (2025): 160900, https://doi.org/10.1016/j.cej.2025.160900.

11. K. Liu, M. Sun, Y. Wu, et al., "Binary Electrolyte Additive-Reinforced Interfacial Molecule Adsorption Layer for Ultra-Stable Zinc Metal Anodes," *Advanced Materials* 37 (2025): 2420079, https://doi.org/10.1002/adma.202420079.

12. T. Li, H. Yang, X. Dong, et al., "Co-Regulation of Interface and Bulk for Enhanced Localized High-Concentration Electrolytes in Stable and Practical Zinc Metal Batteries," *Angewandte Chemie International Edition* 64 (2025): 202501183, https://doi.org/10.1002/anie.202501183.

13. Y. Qiu, Y. Lin, D. Shi, et al., "Möbius Solvation Structure for Zinc-Ion Batteries," *Advanced Materials* 37 (2025): 2415373, https://doi.org/10.1002/adma.202415373.

14. M. Zhao, X. Chen, S. Liu, et al., "Zwitterion-Functionalized Gel Electrolyte Via Anion-Cation Regulation Enables Rapid Zn^{2+} Kinetics for Low-Temperature Zinc Batteries," *Chemical Engineering Journal* 527 (2026): 171875, https://doi.org/10.1016/j.cej.2025.171875.

15. R. Zhao, H. Sun, Z. Shen, S. Luo, and Z. J. Xu, "Compact Electrodeposition Enabled by Synchronized Charge Transfer for Stable Aqueous Zn Metal Anodes," *Advanced Functional Materials* 36 (2025): 17609.

16. J. Heo, D. Dong, Z. Wang, F. Chen, and C. Wang, "Electrolyte Design for Aqueous Zn Batteries," *Joule* 9 (2025): 101844, https://doi.org/10.1016/j.joule.2025.101844.

17. Y. Xie, X. Zhou, Y. Guo, et al., "In Situ Constructing Robust Solid-Electrolyte Interphase for Advanced Zn Anode in Acidic Electrolyte," *Small* 21 (2025): 03325, https://doi.org/10.1002/smll.202503325.

18. J. Feng, X. Li, Y. Dong, et al., "Ion-Framework Electrolyte Featured Zinc-Ion Transport for Solvent and Interphasial Co-Passivation," *Advanced Materials* 37 (2025): 2503765, https://doi.org/10.1002/adma.202503765.

19. W. Chen, Y. Wang, F. Wang, et al., "Zinc Chemistries of Hybrid Electrolytes in Zinc Metal Batteries: From Solvent Structure to Interfaces," *Advanced Materials* 36 (2024): 2411802, https://doi.org/10.1002/adma.202411802.

20. P. Cui, T. Wang, Z. Wang, et al., "Co-Solvent Electrolyte-Induced Zinc Anode Surface Reconstruction for High Performance Zinc Ion Batteries," *Chemical Engineering Journal* 500 (2024): 156971, https://doi.org/10.1016/j.cej.2024.156971.

21. P. Hei, Y. Sai, L. Yu, et al., "Cosolvent Electrolyte Design for High-Voltage Aqueous Zinc–Sulfur Batteries," *Journal of the American Chemical Society* 147 (2025): 27802–27811, https://doi.org/10.1021/jacs.5c06710.

22. Z. Zhao, C. Tang, Y. Zhang, et al., "Diethylene Glycol Reduced the Water Activity of Aqueous Electrolyte via Regulating Interphase Chemistry for Highly Durable Zinc-Ion Batteries," *Energy Storage Materials* 70 (2024): 103515, https://doi.org/10.1016/j.ensm.2024.103515.

23. J. Cong, Y. Wang, X. Lin, et al., "Kinetics Compensation Mechanism in Cosolvent Electrolyte Strategy for Aqueous Zinc Batteries," *Journal of the American Chemical Society* 147 (2025): 8607–8617, https://doi.org/10.1021/jacs.4c16880.

24. Q. Guo, W. Mo, J. Huang, and F. Liu, "Reconfiguring the Coordination Structure in Deep Eutectic Electrolytes for Enabling Stable Operation of Zinc-Ion Batteries," *Nano Letters* 24 (2024): 14965–14972, https://doi.org/10.1021/acs.nanolett.4c03480.

25. W. Deng, Z. Deng, Y. Chen, R. Feng, and X. Wang, "Competitive Coordination Structure Regulation in Deep Eutectic Electrolyte for Stable Zinc Batteries," *Angewandte Chemie International Edition* 63 (2024): 202316499, https://doi.org/10.1002/anie.202316499.

26. L. Geng, J. Meng, X. Wang, et al., "Eutectic Electrolyte With Unique Solvation Structure for High-Performance Zinc-Ion Batteries," *Angewandte Chemie International Edition* 61 (2022): 202206717, https://doi.org/10.1002/anie.202206717.

27. Y. Wang, Q. Li, H. Hong, et al., "Lean-Water Hydrogel Electrolyte for Zinc Ion Batteries," *Nature Communications* 14 (2023): 3890, https://doi.org/10.1038/s41467-023-39634-8.

28. C. Meng, W. He, Z. Kong, et al., "Multifunctional Water-Organic Hybrid Electrolyte for Rechargeable Zinc Ions Batteries," *Chemical Engineering Journal* 450 (2022): 138265, https://doi.org/10.1016/j.cej.2022.138265.

29. R. Zhang, W. K. Pang, J. Vongsvivut, et al., "Weakly Solvating Aqueous-Based Electrolyte Facilitated by a Soft Co-Solvent for Extreme Temperature Operations of Zinc-Ion Batteries," *Energy & Environmental Science* 17 (2024): 4569–4581, https://doi.org/10.1039/D4EE00942H.

30. Z. Ou, M. Zhao, K. Zhu, et al., "Constructing Robust Hydrogen Bond Networks in Electrolytes for Long-Life Zinc-Ion Batteries," *Angewandte Chemie International Edition* 138 (2025): 19611.

31. Q. Ren, X. Tang, G. Sun, et al., "Synergetic Structural Optimizations of Zinc Anodes and Electrolytes to Enable Zinc–Iodine Batteries With Excellent Low-Temperature Performances," *ACS Nano* 19 (2025): 29491–29502, https://doi.org/10.1021/acsnano.5c07752.

32. H. Ren, S. Li, L. Xu, et al., "Tailoring Water-in-DMSO Electrolyte for Ultra-Stable Rechargeable Zinc Batteries," *Angewandte Chemie International Edition* 64 (2025): 202423302, https://doi.org/10.1002/anie.202423302.

33. L. Miao, R. Wang, S. Di, et al., "Aqueous Electrolytes With Hydrophobic Organic Cosolvents for Stabilizing Zinc Metal Anodes," *ACS Nano* 16 (2022): 9667–9678, https://doi.org/10.1021/acsnano.2c02996.

34. Y. Xia, Y. Xiao, J. Zhang, Y. Dong, and C.-A. Wang, "Designing Microemulsion Electrolytes With Widened Electrochemical Stability Window for Highly Reversible Aqueous Zinc Ion Batteries," *Advanced Functional Materials* 35 (2025): 2500889, https://doi.org/10.1002/adfm.202500889.

35. L. Yu, J. Huang, S. Wang, L. Qi, S. Wang, and C. Chen, "Ionic Liquid "Water Pocket" for Stable and Environment-Adaptable Aqueous Zinc Metal Batteries," *Advanced Materials* 35 (2023): 2210789, https://doi.org/10.1002/adma.202210789.

36. Q. Sun, "The Hydrophobic Effects: Our Current Understanding," *Molecules* 27 (2022): 7009, https://doi.org/10.3390/molecules27207009.

37. Q. Sun, "The Physical Origin of Hydrophobic Effects," *Chemical Physics Letters* 672 (2017): 21–25, https://doi.org/10.1016/j.cplett.2017.01.057.

38. W. Lv, J. Tao, D. Huang, et al., "In Situ Constructing Hybrid Solid Electrolyte Interphase and Regulating D-Band Center on Zn Substrate to Enable High-Rate and High-Capacity Zn Metal Anodes," *Advanced Functional Materials* 36 (2026): 13857, https://doi.org/10.1002/adfm.202513857.

39. J. Luo, L. Xu, Y. Yang, et al., "Stable Zinc Anode Solid Electrolyte Interphase Via Inner Helmholtz Plane Engineering," *Nature Communications* 15 (2024): 6471, https://doi.org/10.1038/s41467-024-50890-0.

40. D. Wang, D. Lv, H. Peng, et al., "Site-Selective Adsorption on ZnF_2/Ag Coated Zn for Advanced Aqueous Zinc–Metal Batteries at Low Temperature," *Nano Letters* 22 (2022): 1751–1758.

Supporting Information

Additional supporting information can be found online in the Supporting Information section.

Supporting File: adfm76996-sup-0001-SuppMat.docx.